of various test sequences. For a performance comparison of the traffic prediction, the normalised least mean square (NLMS) method [2] was used with the parameters of the best prediction performance and the number of filter taps < 20. A single server FIFO queue was simulated with an RCBR network service model. As in [2], the NLMS-based method renegotiates the bandwidth on a GOP basis and the new channel rate is the predicted bit rate divided by the desired channel utilisation factor (U). No method was used to reduce the number of renegotiations in [2] as, since its performance can depend on the characteristics of video source, this could have degraded the prediction efficiency. This also applied to the proposed method.

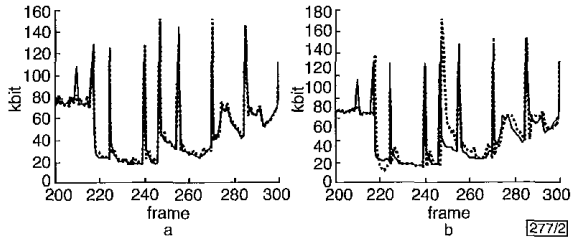

Fig. 2 *Results of traffic prediction for 'mult' sequence*

——— generated traffic
····· predicted traffic

Fig. 2 shows the picture level traffic prediction results of the 'mult' sequence for the proposed and NLMS methods. For a stationary region where there was no scene change, the prediction performance of both methods was nearly the same. However, after scene changes or fast motion, the NLMS method showed a delayed prediction result. In contrast, the proposed method produced quite accurate prediction results through the frame analysis before encoding. As a performance metric, the noise-to-signal ratio of $\Sigma_n(\hat{r}(n) - r(n))^2/\Sigma_n r(n)^2$ was used. The proposed method showed a value of 0.0066 and 0.0043 for the I- and P-pictures, respectively, whereas the NLMS method had a value of 0.0421 and 0.0243. Similar results were also obtained for different sets of quantisation parameters and video sequences.

Table 1: Queue quantile for dynamic bandwidth allocation methods

U	Sequence	0.9 quantile		0.999 quantile	
		NLMS	Proposed	NLMS	Proposed
0.95	cnn	182354	126744	758327	421962
	poet	87765	63670	749664	391637
	tita	248613	95561	700709	651739
0.80	cnn	59770	49355	489315	289140
	poet	38033	35302	576656	248545
	tita	42694	31218	553021	452789

Table 1 shows the queue length quantiles for different utilisation levels for both the proposed and the NLMS-based dynamic bandwidth allocation methods. The results show that the proposed method achieved a queue size reduction of 10 to 60%, in contrast to the NLMS-based method. With a smaller queue size, less queueing delay is expected, which is desirable for real-time video applications. In addition, since these results did not include the effect of the renegotiation delay, a further queue increase is expected for both methods owing to a rate mismatch until the new traffic parameter is active. However, the queue increase of the proposed method is still expected to be less than that of the conventional, since the proposed method can accurately detect and predict any changes in the source traffic before encoding.

In conclusion, by using source information, it is possible to accurately detect changes in source traffic and predict the bit rate of video frames before encoding, whereas conventional methods can only do this using the bit rate history of encoded frames. Simulation results show that the proposed method achieves a better prediction and requires a smaller buffer in RCBR service than the conventional method.

11 September 2000
Electronics Letters Online No: 20001447
DOI: 10.1049/el:20001447

Myeong-jin Lee and Jae-kyoon Kim (*Department of Electrical Engineering, Korea Advanced Institute of Science and Technology, 373-1 Kusong-dong, Yusong-gu, Taejon 305-701, Korea*)

E-mail: mjlee@vispop.kaist.ac.kr

References

1 GROSSGLAUSER, M., KESHAV, S., and TSE, D.: 'RCBR: A simple and efficient service for multiple time scale traffic'. ACM SIGCOMM, 1995, pp. 219–230

2 ADAS, A.: 'Using adaptive linear prediction to support real-time VBR video under RCBR network service model', *IEEE/ACM Trans. Netw.*, 1998, **6**, (5), pp. 635–644

3 CHONG, S., LI, S., and GHOSH, J.: 'Predictive dynamic bandwidth allocation for efficient transport of real-time VBR video over ATM', *IEEE J. Sel. Areas Commun.*, 1995, **13**, (1), pp. 12–23

Dual carrier suppression interferometer for measurement of phase noise

E. Rubiola and V. Giordano

A new scheme for phase noise measurement is presented, based on dual stage suppression of the carrier and synchronous detection of the noise sidebands of the device being tested. This scheme features real time output and intrinsically low instrument flicker. A prototype shows a residual flicker as low as –160dBrad²/Hz at 1Hz off the 100MHz carrier. Other implementations are possible, from 1MHz to several gigahertz. Applications include the noise characterisation of components and the design of innovative ultrastable oscillators.

Introduction: Phase noise is generally described in terms of the power spectrum density $S_\varphi(f)$ of the phase fluctuation $\varphi(t)$, as a function of the Fourier frequency f. This refers to a nearly perfect sinusoidal signal of carrier frequency ν_0 of the type $s(t) = V_o[1 + \alpha(t)]\cos[2\pi\nu_0 t + \varphi(t)]$; in the field of frequency metrology, the amplitude fluctuation $\alpha(t)$ is often regarded as a minor problem.

Flicker noise is probably the most difficult challenge in the design of precision oscillators. In fact, according to the well-known Leeson model [1], the oscillator turns the phase flicker of its internal components into frequency flicker ($S_\varphi(f) \propto f^{-3}$), which is a divergent process in the time domain. This Letter proposes an innovative phase noise measurement instrument designed to obtain the lowest residual flicker, intended for the measurement of components or for active noise removal, and reports on a prototype that proves the benefits of the method.

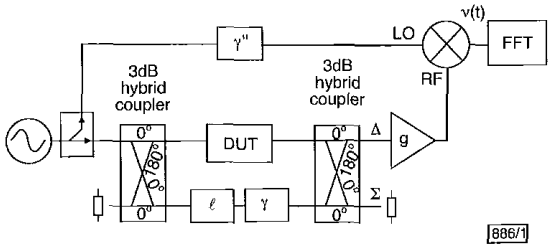

Fig. 1 *Block diagram of interferometric setup for measurement of phase noise*

Radiofrequency interferometer: The interferometric setup for the measurement of phase noise is analysed in-depth in [2], together with the design rules and experimental results. In short, with reference to Fig. 1, setting the attenuator ℓ and the phase shifter γ' equal to the phase and attenuation of the device under test (DUT), the carrier is suppressed at the Δ port of the second 3dB hybrid coupler. Therefore, only the DUT noise sidebands are present at the input of the amplifier. These sidebands are amplified, downconverted to baseband, and measured by a fast Fourier transform (FFT) analyser. Properly setting γ'', the output voltage

is $v(t) = k_\varphi \varphi(t)$, from which $S_\varphi(f) = S_v(f)/k_\varphi^2$. The phase-to-voltage gain is $k_\varphi = \sqrt{(R_0 g P_o/\ell_h \ell_m)}$, where R_0 is the characteristic impedance of the circuit, g is the amplifier gain, P_o is the DUT output power ($P_o = V_o^2/2R_0$), ℓ_h is the hybrid loss and ℓ_m is the SSB loss of the mixer. Furthermore, the white noise floor of the instrument, as observed bypassing the DUT, is $S_{\varphi 0} = 2\ell_h F k_B T_0/P_o$, where F is the noise figure of the amplifier and $k_B T_0 \simeq 4 \times 10^{-21}$J is the thermal energy at room temperature.

The scheme shown in Fig. 1 is derived from [3, 4].

Dual carrier suppression scheme: Generally, the flicker of the instrument (Fig. 1) can be minimised by keeping the residual carrier at the amplifier output as low as possible. This rule derives from the simple observation that the close-to-the-carrier $1/f$ noise of the amplifier comes from the near-DC flicker upconverted by the carrier-induced nonlinearity, and that if no carrier was present the radiofrequency noise spectrum would be flat around that frequency. The flicker modulation tends to arise from the output stage of the amplifier, where the residual carrier is stronger.

However, the flicker noise of the interferometer still remains, regardless of how low the residual carrier is. This is mainly due to the mechanical instability of the variable devices ℓ and γ', which induce random modulation. No advantage results from replacing these devices with electrically controlled attenuators and phase shifters, generally more noisy than the mechanically tunable ones.

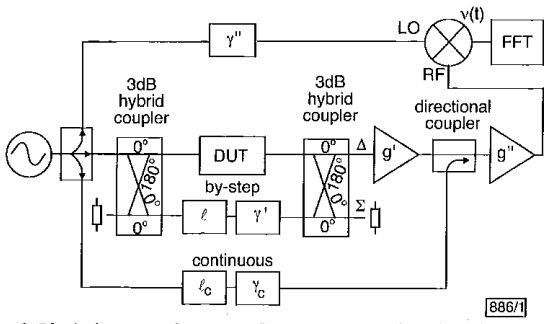

Fig. 2 *Block diagram of new interferometric setup, based on dual carrier suppression*

Experience and common sense suggest that by-step variable attenuators and phase shifters are more stable than continuous ones. Unfortunately, they cannot be exploited in Fig. 1 because the step attenuation of the actual devices limits the carrier suppression to ~45dB, which is not sufficient according to the design rules given in [2]. This problem is overcome in the dual carrier suppression scheme of Fig. 2. The carrier is first attenuated by some 40–45dB in the inner interferometer; this involves the by-step attenuator ℓ, the phase shifter γ' and the two hybrids. The DUT noise sidebands, together with the residual carrier, are amplified by a first stage. Then, the carrier is almost completely suppressed in the outer interferometer by injecting a suitable signal at the output of the first amplifier; this involves the continuous attenuator ℓ_c, the phase shifter γ_c, and the directional coupler. Finally, the DUT noise is further amplified and detected as in the previous scheme. The key points are: (i) the first amplifier is prevented from flickering by ensuring its fully linear operation despite the carrier being only partially suppressed; this is done by choosing a device that exhibits a wide dynamic range and a relatively low gain; (ii) the output noise of the continuous attenuator and phase shifter, referred at the DUT output, is divided by $2\ell_h g'(k_c - 1)$, where k_c is the attenuation parameter of the directional coupler; for the sake of simplicity, the dissipative loss of the latter is not considered.

Experimental results: The prototype we experimented on is designed to operate at the carrier frequency ν_c = 100MHz. The inner interferometer is based on a 0.1dB step attenuator, whose range can be extended with external fixed-value attenuators, and on a set of semirigid cables that play the role of γ'. The hybrid loss is ℓ_h = 1dB, and the gain of the first amplifier is g' = 11.8dB. The total gain along the 100MHz amplifier chain is 36.5dB, including the 3.5dB loss of a monitor tap, not shown, at the output of the second amplifier; the noise figure is F = 2dB. The directional coupler of the outer interferometer shows a coupling factor k_c = 11.4dB. Consequently, the rejection of the continuous attenuator and phase shifter noise is $2\ell_h g'(k_c - 1)$ = 26.9dB. The mixer, which also includes a 10MHz lowpass filter to remove the $2\nu_c$ component, shows an SSB loss of 6dB. The FFT analyser is preceded by a 40dB low noise preamplifier, not shown. The 100MHz source is a high-stability oven-controlled quartz oscillator followed by a power amplifier.

Calibration is straightforward. The carrier suppression is set first by inspecting the inner interferometer alone and acting on ℓ and γ', and then by restoring the final configuration and adjusting ℓ_c and γ_c to obtain the lowest carrier power at the amplifier output. γ'' is set through a zero method that consists of nulling the response to a reference phase modulation, and adding a calibrated 90° lag. Obviously, the same phase modulation is also used for the direct measurement of k_φ. A carrier suppression of 80–90dB can be obtained, stable for about one hour. Operating with a DUT power P_o = 7.8dBm, our prototype shows an overall gain of = 64.6dBV/rad, from the DUT to the preamplifier output.

Our main interest is the flicker noise of the instrument. Thus, we measured the residual noise spectrum $S_\varphi(f)$ in the absence of a DUT, which is bypassed. Fig. 3 shows the result, averaged over 60 acquisitions. The white noise is –175.3dBrad²/Hz, which is close to the predicted value of –175.8dBrad²/Hz. The flicker noise is $S_\varphi(1\text{Hz})$ = –160.3dBrad²/Hz, which represents an improvement of some 10dB over preceding instruments [2]. Under the same conditions but setting γ'' for the detection of amplitude noise, the residual white noise remains substantially unchanged, and the residual flicker noise is $S_\alpha(1\text{Hz})$ = –161.2dB(V²/V²)/Hz.

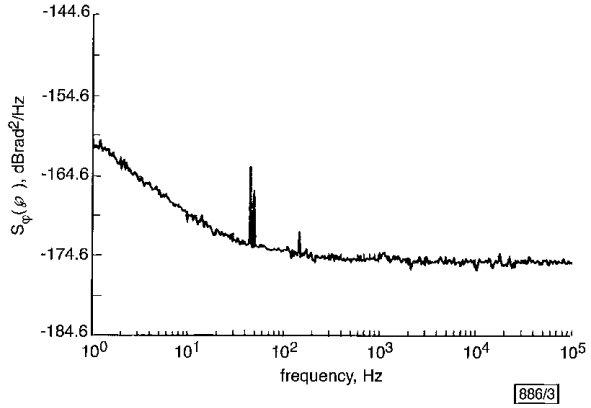

Fig. 3 *Residual noise of instrument measured bypassing device under test*

Final remarks: We wish to stress that no attempt has been made to hide the spectral lines due to mechanical vibrations and to the interferences from the mains, and that a moderate averaging has no effect on them. The low level of these stray signals shown in Fig. 3 is due: (i) to a good mechanical assembly; (ii) to the intrinsic immunity to the low frequency magnetic fields derived from the amplification of the noise sidebands before detecting; and (iii) to the increased stability that results from having removed the continuously variable attenuator and phase shifter from the critical path.

The described instrument measures the instant value of $\varphi(t)$ in real time, which can be exploited for the dynamic correction of the noise of oscillators, as suggested in [5] for microwave applications.

Similar results are expected over a wide frequency range, from 1MHz or less to several gigahertz, where the same technology is available. Higher frequency implementations seem feasible, once problems related to the phase shifter γ' are solved.

20 October 2000
Electronics Letters Online No: 20001476
DOI: 10.1049/el:20001476

E. Rubiola (*ESSTIN, Université Henri Poincaré, Nancy 1, 2, rue Jean Lamour, F-54519 Vandoeuvre Les Nancy, France*)

E-mail: rubiola@esstin.uhp-nancy.fr

V. Giordano (*Laboratoire de Physique et Metrologie des Oscillateurs (LPMO), 32 av. de l'Observatoire, F-25044 Besançon, France*)

E. Rubiola: Also with LPMI-CNRS, Faculté des Sciences, Bld. des Aiguillettes, F-54506 Vandoeuvre Les Nancy, France

References

1 LEESON, D.B.: 'A simple model of feed back oscillator noise spectrum', *Proc. IEEE*, 1966, **54**, pp. 329–330

2 RUBIOLA, E., GIORDANO, V., and GROSLAMBERT, J.: 'Very high frequency and microwave interferometric PM and AM noise measurements', *Rev. Sci. Instrum.*, 1999, **70**, (1), pp. 220–225

3 SANN, K.H.: 'The measurement of near-carrier noise in microwave amplifiers', *IEEE Trans. Microw. Theory Technol.*, 1968, **16**, (9), pp. 761–766

4 LABAAR, F.: 'New discriminator boosts phase noise testing', *Microw.*, 1982, **21**, (3), pp. 65–69

5 IVANOV, E.N., TOBAR, M.E., and WOODE, R.A.: 'Microwave interferometry: applications to precision measurements and noise reduction techniques', *IEEE Trans. Ultrason. Ferroelectr. Freq. Control*, 1998, **45**, (6), pp. 1526–1536

Room temperature operation of GaAsSb/GaAs quantum well VCSELs at 1.29μm

F. Quochi, J.E. Cunningham, M. Dinu and J. Shah

Room temperature pulsed lasing at 1.29μm in an optically pumped GaAsSb/GaAs quantum well VCSEL on a GaAs substrate is reported. This is the longest wavelength VCSEL reported in this material system.

Introduction: Vertical-cavity surface-emitting lasers (VCSELs) emitting at 1.3μm at and above room temperature are attracting more and more interest for optical communications. Various GaAs-based material systems are currently being investigated in VCSELs with very high-Q-factor microcavities made of AlGaAs/GaAs and GaAs/AlO distributed Bragg reflectors (DBRs). Among these are InAs quantum dots (QDs) [1], InGaAsN [2] and GaAsSb [3] quantum wells (QWs). Other material systems are also utilized as active media inside AlGaAs/GaAs microcavities, e.g. InGaAsP/InP QWs [4]. First demonstrations of an InAs/GaAs QD VCSEL operating at 1.3μm has been reported very recently [5]. To date, lasing in InGaAsN QW VCSELs has been demonstrated up to 1.294μm [6], while the record of long wavelength emission in GaAsSb QW VCSELs is 1.23μm [7]. 1.3μm lasing of the GaAsSb/GaAs system has been reported only in edge-emitting devices [8]. In this Letter, we show pulsed lasing in an optically pumped GaAsSb/GaAs QW VCSEL grown on a GaAs substrate and designed to emit at 1.29μm, at room temperature. The lasing wavelength 1.29μm is the longest yet reported in GaAsSb QW VCSELs.

Experiment: Fig. 1 depicts the cross-sectional diagram of the VCSEL and the optical excitation/detection geometry. The sample is grown by molecular-beam epitaxy on a GaAs substrate. It consists of two 6nm-wide $GaA_{0.7}Sb_{0.3}$ QWs embedded in a λ-thick GaAs microcavity. The QWs are positioned symmetrically with respect to the centre of the GaAs spacer, and are separated by 35nm. The bottom (top) mirror is an AlGaAs/AlAs (SiO_2/TiO_2) DBR made of 27.5 (11) λ/4-thick pairs. The microcavity is designed for $\lambda \simeq 1.29\mu m$. The device is optically pumped through the top mirror by a CW Ti:Sapphire laser tuned at 810nm, which is focused down to an 8μm-diameter spot on the sample. We use an acoustic-optical modulator on the laser beam to achieve pulsed excitation of variable duration and repetition time. The vertical emission through the substrate (which is anti-reflection coated to avoid extra optical feedback) is collected, dispersed in a single pass spectrometer, and detected by an N_2-cooled InGaAs-array detector. The average output power is measured with a power meter with 1nW sensitivity at ~1.3μm. As for the following results, 1μs-long pulses were used to excite the device. The repetition time was varied in the 3–100μs range.

Results: The optical response of the device at room temperature is shown in Fig. 2. Data refer to an emission wavelength of 1288nm. Output power is measured with collection f-number equal to 2. With a repetition time of 10μs we observe a laser characteristic with threshold peak (absorbed) power $P_{th} \simeq 20$mW and differential quantum efficiency η ($= \Delta P_{out}/\Delta P_{in} \simeq 4.5 \times 10^{-3}$ (line with dots). Taking into account the emission through the top mirror, we estimate the total differential quantum efficiency to be $\sim 9 \times 10^{-3}$. The peak output power (at 71mW peak excitation power) is 215μW (21.5μW average). The emission spectrum is displayed in the inset of Fig. 2 for peak excitation power of 22mW (10% above threshold). Measurements with longer repetition times (up to 100μs) show that average heating at 10μs period is negligible. By contrast, when the period is shortened down to 3μs, average heating results in a visible degradation of the optical performance (line with triangles).

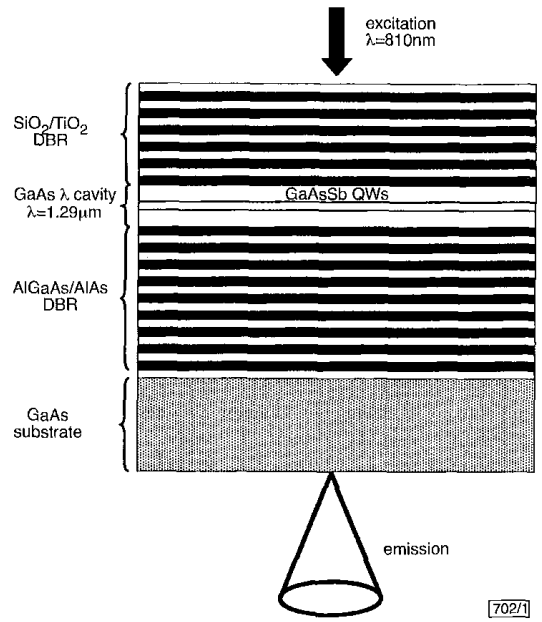

Fig. 1 *Schematic diagram of VCSEL structure with geometry of optical excitation/emission*

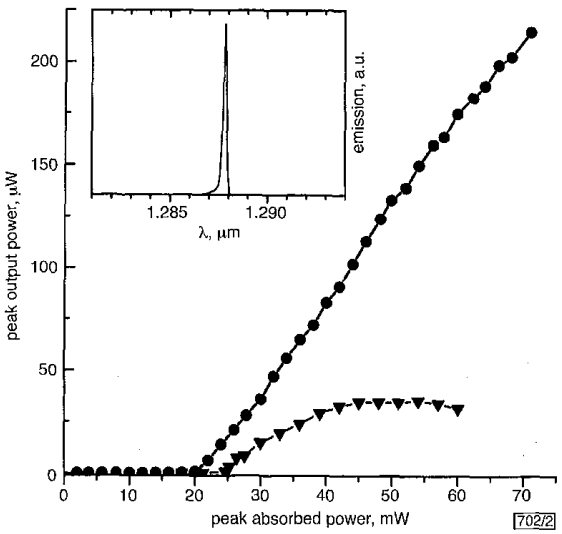

Fig. 2 *Room temperature VCSEL characteristic at 1288nm, for 1μs excitation duration with different repetition times*

—●— 10μs repetition time
—▼— 3μs repetition time
Inset: Lasing spectrum for peak absorbed power = 22mW

The emission wavelength of the device is tunable to some degree (~10nm), owing to the nonuniformity of the microcavity thickness across the sample. Lasing action with 10μs-period excitation was achieved up to the record value of 1292nm. The threshold at 1292nm is however twice as large and the differential quantum efficiency 5 times smaller than at 1288nm. Optical studies in other samples having the same structure but with the Fabry-Pérot mode